Nature of the Active Ni State for Photocatalytic Hydrogen Generation

Jasmin S. Schubert, Eva Doloszeski, Pablo Ayala, Stephen Nagaraju Myakala, Jakob Rath, Bernhard Fickl, Ariane Giesriegl, Dogukan H. Apaydin, Bernhard C. Bayer, Shun Kashiwaya, Alexey Cherevan,* and Dominik Eder*

Thermal treatments can have detrimental effects on the photocatalytic hydrogen (H_2) evolution performance and impact the formation mechanism of the active state of surface-supported co-catalysts. In this work, a range of Ni-based co-catalysts is investigated immobilized on TiO_2, evaluated their H_2 evolution rates in situ over 21 h, and analyzed the samples at various stages with a comprehensive set of spectroscopic and microscopy techniques. It is found that achieving the optimal hydrogen evolution (HER) performance requires the right Ni^0:Ni^{2+} ratio, rather than only Ni^0, and that Ni needs to be weakly adsorbed on the TiO_2 surface to create a dynamic state. Under these conditions, Ni can undergo an efficient redox shuttle, involving the transformation of Ni^{2+} to Ni^0 and back after releasing the accumulated electrons for H^+ reduction (i.e., $Ni^{2+} \leftrightarrow Ni^0$). Yet, when the calcination temperature of the Ni/TiO_2 photocatalysts increases, resulting in stronger coordination/adsorption of Ni on TiO_2, this process is gradually inhibited, which ultimately leads to decreased HER performances. This work emphasizes the significance and influence of thermal treatments on the Ni active state formation – a process that can be relevant to other HER co-catalysts.

J. S. Schubert, E. Doloszeski, P. Ayala, S. N. Myakala, J. Rath, B. Fickl,
A. Giesriegl, D. H. Apaydin, B. C. Bayer, A. Cherevan, D. Eder
Institute of Materials Chemistry
Technische Universität Wien (TU Wien)
Getreidemarkt 9, Vienna 1060, Austria
E-mail: alexey.cherevan@tuwien.ac.at; dominik.eder@tuwien.ac.at
S. Kashiwaya
Materials Design
Department of Physics
Chemistry
and Biology (IFM)
Linköping University
Linköping 58183, Sweden

1. Introduction

Photocatalysis utilizes the energy of light under ambient and environmentally friendly conditions to enable and accelerate thermodynamically challenging processes, such as overall water splitting for light-driven hydrogen (H_2) production.[1,2]

The photocatalyst architecture plays a key role in the ultimate performance and, currently, the most efficient and longevous photosystems are still based on heterogeneous materials.[1–5] This approach combines solid-state semiconductors – able to absorb light, generate electron-hole pairs and transfer their energy to the catalytic sites – and other materials, such as co-catalysts, that offer active sites to promote specific reactions. The combination can greatly improve the separation of photoexcited charge carriers and their transfer into adsorbed reactant species, enhancing the overall photocatalytic activity.[1,2,5,6] Consequently, co-catalyst engineering to optimize photocatalytic efficiencies of the reaction of interest has become a popular research focus.

The light-to-hydrogen conversion efficiency is governed by the degree of electronic communication between the semiconductor and co-catalyst, structural characteristics of their interfaces as well as the accessibility of the catalytically active sites.[1–3,5,7–9] Much effort has been dedicated to designing the ideal co-catalyst/semiconductor interface through various bottom-up methods such as photo-deposition, chemical deposition, and growth and selective surface reaction.[10–14] In many cases, co-catalysts are further activated through post-synthetic modifications, for example by irradiation or thermal treatment in oxidative/reductive environments. However, these conditions can also facilitate the growth and agglomeration of co-catalyst-nanoparticles or instigate changes in their chemical interaction with the substrate.[10,12,15] Consequently, it is crucial to understand how these treatments affect the electronic, chemical, and structural characteristics of the co-catalyst species, the accessibility of the catalytic sites, the potential formation of charge recombination centers along with localized inter-bandgap states

**ADVANCED
SCIENCE NEWS**

www.advancedsciencenews.com

**ADVANCED
MATERIALS
INTERFACES**

Open Access

www.advmatinterfaces.de

at the interfaces, and – ultimately – the resulting photocatalytic performance.[3,5,7–9]

In this context, the utilization of Ni as a co-catalyst has been widely documented across various systems, encompassing diverse chemical compositions (Ni^0, $Ni(OH)_2$, NiO, NiS_2, Ni_2P, etc), substrates (TiO_2, CdS, g-CN, MoS_2, etc) and synthesis methods, all with the overarching aim of enhancing photocatalytic performance.[16–18] Numerous studies have made concerted efforts to unravel the catalytic active state of Ni. For instance, Chen et al.[19] observed that the prior reduction of NiO to Ni^0 – when deposited on a TiO_2 substrate – results in a remarkable augmentation in the quantity of H_2 produced. Furthermore, under photocatalytic conditions they observed a long induction time for the NiO/TiO_2 sample, revealing that NiO gets gradually reduced to Ni^0. Accordingly, they concluded that the catalytically active form of Ni is Ni^0. Indra et al.[20] obtained analogous results using in-situ EPR by photodepositing Ni on graphitic carbon nitride (g-CN). The authors demonstrated that photo-excited electrons in the g-CN's conduction band are responsible for reducing Ni^{2+} to Ni^0 and subsequently catalyzing the conversion of H^+ to H_2. Hence, again metallic Ni was suggested as an H_2 generating center. Additionally, the authors observed the formation of metallic Ni only under photocatalytic conditions, hereby coexisting Ni^{2+} and metallic Ni in the whole process. Yu et al.[21] conducted an investigation involving $Ni(OH)_2$ on TiO_2 and reached the same conclusion. In a separate study, Lv et al.[22] utilized a multitude of methods to clarify that Ni is affixed to the TiO_2 lattice in the form of Ni^{2+}-O. Once again, they asserted that the excited electrons in the conduction band are the key players in H_2 production, though they did not specify whether Ni^{2+} is reduced or if Ni actively partakes in the reaction. In our previous study,[23] we also showed how the amount of H_2 produced increased gradually over time when using NiO_x/TiO_2 photocatalyst, which correlated well with a gradual increase of the amount of Ni^0/Ni^{2+} proportion.

In summary, there is a prevailing consensus that photoexcited electrons migrate from the conduction band to the attached Ni species, leading to the formation of metallic Ni.[16–25] This species, in turn, can react with protons to generate H_2, thus establishing Ni^0 as the active form for photocatalytic H_2 generation. However, as many reported photocatalytic systems contained a mixture of Ni^0 and Ni^{2+} states, the precise extent to which metallic Ni and/or Ni^{2+} contribute to the activity trends, as well as the distinct roles played by each of the Ni oxidation states, remain unaddressed questions. Consequently, further research is imperative to comprehensively unravel the roles played by different Ni oxidation states as well as the effect of photocatalyst synthesis and post-treatments in achieving maximum performances.

In this work, we examine a series of Ni-based co-catalysts supported on TiO_2 – chosen as model support – and provide a comprehensive insight into the effects of thermal pre-treatments on their structure-property-photocatalytic performance relationships. Using a wide range of techniques, we observe surprising detrimental effects of heat treatments on their photocatalytic performance towards HER. We also unravel the underlying structural, electronic, and mechanistic contributions that govern the activity of the photocatalytic reaction and identify the redox activity of Ni/Ni^{2+} and the strength of their coordination to the TiO_2 surface as key criteria.

2. Results and Discussion

Ni was deposited on TiO_2 from nickel (II) acetylacetonate ($Ni(acac)_2$) via wet impregnation followed by different post-synthesis treatments including room temperature (RT) drying – that is, no thermal treatment – as well as calcination at 250°C and 400°C (Ni/TiO_2 samples). Additionally, a benchmark Ni/TiO_2 composite was also prepared via in situ photo deposition (PD) of Ni from $Ni(acac)_2$.[10,11,26–28] The photocatalytic performance of the catalysts was evaluated using H_2 detection in-flow with high temporal resolution (see experimental section). Furthermore, three different Ni/TiO_2 sample sets were prepared to explore the impact of synthetic solvents (i.e., H_2O or EtOH) and the influence of atmospheric O_2 on Ni deposition (i.e., ambient and vacuum conditions). In addition, Ni-free benchmark TiO_2 samples: non-calcined (RT) and the one calcined at 400°C – were investigated to account for the effect of calcination on its crystallinity and defect level (see Figure S2). Since all sample sets showed similar performance trends independent of these synthetic aspects, and because the highest photocatalytic activity was obtained for the Ni/TiO_2 samples derived from the EtOH-based synthesis in vacuo (further details on the synthesis and discussion about the sample sets are in SI section 3), for simplicity, we focus here on the representative set of Ni/TiO_2 samples prepared via wet impregnation using EtOH/vacuum conditions.

For each experiment, two illumination periods were carried out (highlighted in **Figure 1**a yellow): a short-term period (the 1 h of illumination) which corresponds to the activation cycle of the photocatalyst, and a long-term period (a follow-up 17 h illumination) which allows us to uncover steady-state activity trends and discuss (de)activation behavior. Additionally, we analyzed the CO_2 evolution rates in situ (Figure 1b) aiming to obtain additional insight into the oxidative behavior of Ni/TiO_2 photocatalysts.

H_2 profiles – Activation cycle (Figure 1a): The RT and PD samples show the sharpest evolution rate increase after illumination starts. Yet, after 18 min of illumination (a in Figure 1a), the PD sample reaches the H_2 evolution rate maximum, while RT continues to increase. The 250 and 400°C calcined samples, show a gradual activation rate decrease by 66.7% and 83.3%, respectively, when compared to the HER profile of the RT sample. After 1 h of illumination, the total amount of H_2 generated is 39.1 and 32.9 µmol for RT and PD samples, and 26.7 and 15.4 µmol for the samples derived at 250 and 400°C, respectively. Hereby, the data clearly show that increasing the calcination temperature leads to a slower HER rate increase and an overall diminished H_2 generation after 1 h of illumination.

H_2 profiles – Stability cycle: The HER rate slightly increases for the RT sample and reaches a maximum after a total illumination of ~10 h (b in Figure 1a). For the samples calcined at 250 and 400°C, the HER rate maximum is reached earlier, already after a total illumination time of 1.5 h (c in Figure 1a) and 2.5 h (d in Figure 1a), respectively. The HER profile of the PD sample generated in situ under photocatalytic conditions is reminiscent of the RT sample. These results suggest that the RT and PD samples constitute similar composition and structure of the active state. The different activation behaviors are likely of kinetic origin, as in the case of the PD sample Ni/TiO_2 formation requires a rather slow deposition of Ni species from the solution. In contrast, the RT sample already has $Ni(acac)_2$ present on the TiO_2 surface after
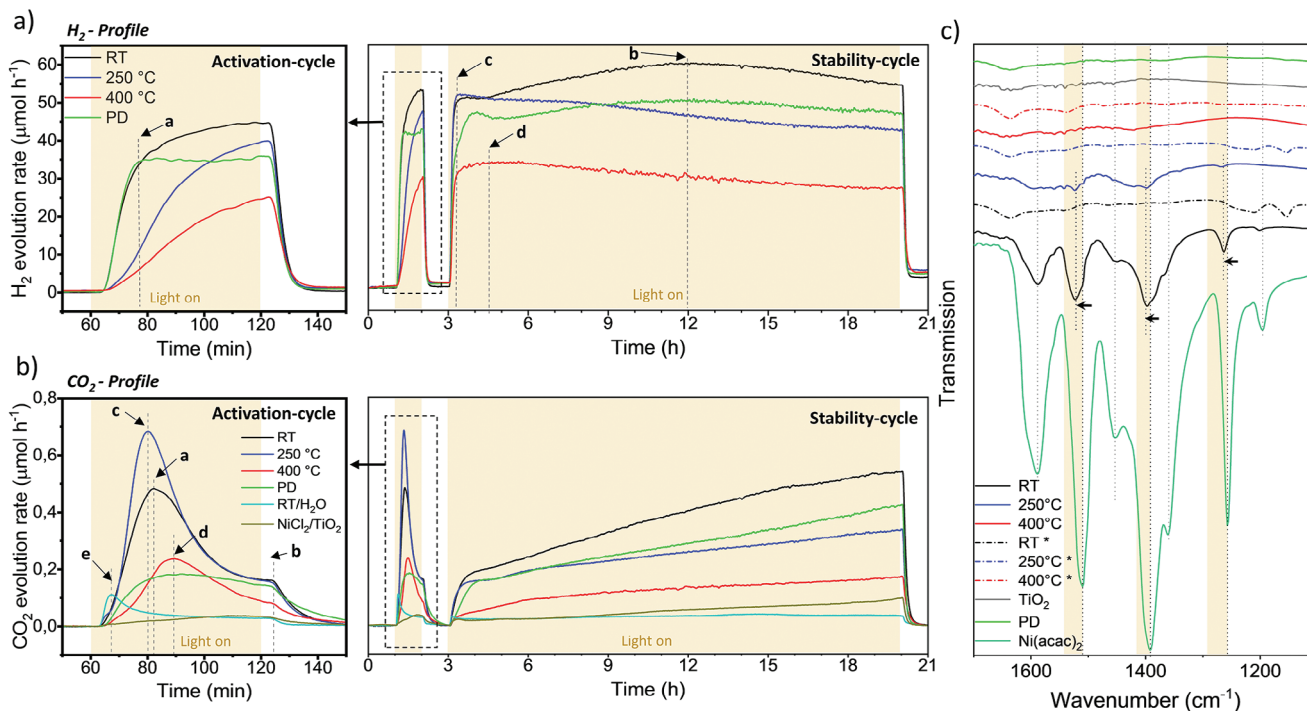
**ADVANCED
SCIENCE NEWS**

www.advancedsciencenews.com

**ADVANCED
MATERIALS
INTERFACES**
Open Access

www.advmatinterfaces.de

Figure 1. a) Hydrogen evolution reaction (HER) rate profile and b) CO_2 evolution rate profile of different Ni/TiO_2 calcined samples (non-calcined (RT), and calcined at 250 and 400°C), photo deposited Ni/TiO_2 sample (PD), RT sample tested only in water (i.e., without a sacrificial agent, MeOH, RT/H_2O) and $NiCl_2/TiO_2$ sample. Zoom-in of the first 3 h HER (the activation cycle) and full 21 h HER profile (showing the activation- and stability cycle) are shown on the left and right, respectively. The illumination (light-on) periods are indicated by the yellow shading. Some points of interest, which are referred to in the main text, are indicated with letters a-d. The total amount of H_2 generated (i.e., the integrated area) and the activation slope values are summarized in Table S2. The corresponding HER profiles of the RT/H_2O and $NiCl_2/TiO_2$ are shown in Figure S9. The short delay between the start of illumination and the rise of the hydrogen signal is due to the experimental setup (see experimental section). c) FTIR-ATR before and after HER for the Ni/TiO_2 samples, PD, $Ni(acac)_2$, and TiO_2. * Spectra acquired for the samples after photocatalysis. Full-range FTIR-ATR spectra are shown in Figure S10.

the synthesis, which facilitates a faster generation of HER-active Ni centers by the photoexcited electrons.[19,21] The ability of Ni species to extract electrons from TiO_2 was further demonstrated by chronoamperometry measurements (Figure S8). Overall, the data show that thermal treatments result in a gradual HER rate decline that increases with calcination temperature and leads to different activation/deactivation behaviors.

CO_2 profiles – Activation cycle (Figure 1b): For the RT sample, the CO_2 evolution reaches a maximum at ~22 min of illumination (a in Figure 1b), after which it drops abruptly by 71.7% (b in Figure 1b). The samples calcined at 250 and 400°C show similar CO_2 evolution profiles. However, the 250°C sample generates much more CO_2 (peaking after 20 min of illumination, c in Figure 1b), while the 400°C sample's CO_2 peak maximum appears considerably later and is less intense (peaking after ~30 min of illumination, d in Figure 1b). The major contribution to CO_2 generation is due to the oxidation of MeOH, which is used here as a sacrificial agent.[29–31] However, the presence of metalorganic precursors on the catalyst's surface, that is, $Ni(acac)_2$, is expected to contribute to CO_2 generation as well upon oxidation during the initial stage of the photocatalytic process. Accordingly, we analyzed the samples by attenuated total reflectance Fourier transform infrared spectroscopy (ATR-FTIR) before and after photocatalysis (Figure 1c). Before photocatalysis, the RT sample features vibrational bands that correspond well to

the fingerprint of $Ni(acac)_2$, with noticeable shifts of some signals (1512.1 to 1523.7 cm^{-1}, 1390.6 to 1400.2 cm^{-1} and 1257.5 to 1265.2 cm^{-1}), indicating strong interaction of the acac ion with the TiO_2 surface.[23,32] After calcination at 250 and 400°C, the acac intensities gradually decrease by increasing temperature. After photocatalysis, the acac bands completely vanish in all samples. Two possibilities can explain these observations: dissolution of the acac ion into the reaction solution and/or complete decomposition of the acac anion by the photocatalytic process. Washing experiments of the RT sample complemented by FTIR-ATR analyses before and after (see Figure S10) show that acac is weakly attached to the TiO_2 surface, suggesting that acac gets dissolved into the reaction solution. To further confirm the origin of the CO_2 peaks and the role of the acac anion, we performed two additional benchmark experiments. In the first, we synthesized a sample following an identical synthetic procedure but using an all-inorganic $NiCl_2$ as a precursor ($NiCl_2/TiO_2$), that is, the only organic source in the reaction was MeOH. The respective evolution curve clearly shows no peak formation, just a steady slow increase in CO_2 (Figure 1b). In the second experiment, we used $Ni(acac)_2$ as the precursor but performed the reaction only in water without MeOH (RT/H_2O). Here, the corresponding CO_2 profile shows a sharp evolution peak that drops quickly to almost no CO_2 formation. These data confirm that the observed peak in the 1 h of illumination directly relates to the oxidation of the
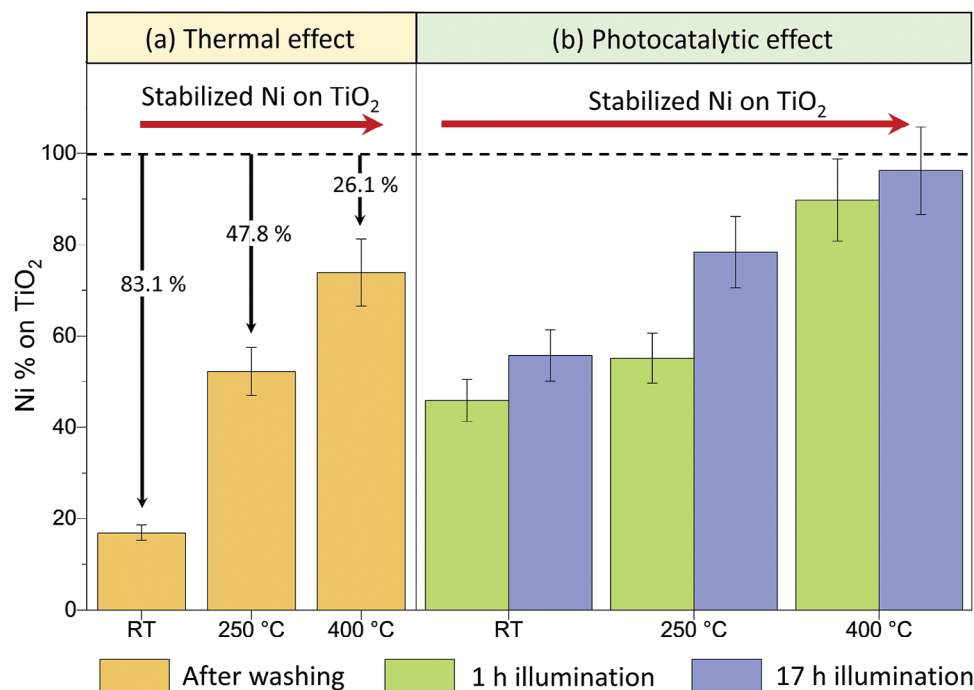
Figure 2. Total Ni % in the Ni/TiO$_2$ samples –, that is, stabilized Ni on TiO$_2$ – a) after washing of the as-prepared samples (see experimental section for more details) as well as b) those after photocatalysis (the activation- (1 h illumination) and stability-cycle (after 17 h illumination)). The relative Ni content values were calculated from the as-synthesized samples set as 100% (see Table S3).

metalorganic precursor or its decomposition intermediates (as seen in ATR-FTIR for the 250 and 400°C samples).

CO$_2$ profiles – Stability cycle (Figure 1b): all Ni/TiO$_2$ samples show a steady increase in the CO$_2$ evolution rate over time. The activity trend correlates well with the HER rate trend according to RT >250°C >400°C. The PD sample, again, shows a reaction profile similar to that of the RT sample, but with a lower maximum rate – expected from its lower HER activity – thus further indicating a similar reaction mechanism. The gradual increase of the CO$_2$ evolution rate over time observed for all samples is related to the conversion of MeOH. The more MeOH and its decomposition intermediates accumulate over time, the stronger the equilibrium shifts to CO$_2$.

2.1. Ni on TiO$_2$ Attachment Strength

To gain information about the thermal and photocatalytic effects on the Ni adsorption/coordination strength with the TiO$_2$ surface, we quantified the Ni amount present in the as-synthesized samples, after washing them (details in experimental section), as well as after the activation- and stability-cycles (i.e., after 1 and 17 h illumination, HER experiment) (**Figure 2**). For the as-synthesized Ni/TiO$_2$, X-ray fluorescence (XRF) confirms that the content of Ni is close to the expected 5 at% for all samples independent of the thermal treatment (for more details see Table S3). After washing, 83.1% of the original Ni amount present in the RT sample got washed off, whereas much less of Ni – 47.8 and 26.1% – was detached from the samples calcined at 250 and 400°C, respectively (see black arrows in Figure 2a). These values clearly

show that calcination at higher temperatures results in stronger adhesion/adsorption of Ni species to TiO$_2$ involving stronger coordination of Ni species to the TiO$_2$ lattice and partial formation of oxy/hydroxide-like species at the TiO$_2$ surface (for more details, see -OH bands in ATR-FTIR shown in, Figure S10). For the samples after HER, after the activation cycle (1 h illumination in Figure 2b), the residual amounts of stabilized Ni on TiO$_2$ – for the initial Ni contents – amount to 45.9, 55.1 and 89.8% for RT, 250 and 400°C, respectively. In contrast, the respective Ni content after the stability cycle (17 h illumination in Figure 2b) remains significantly higher with 55.7, 78.3, and 96.2% for RT, 250, and 400°C, respectively. This shows that the adhesion of Ni on the TiO$_2$ surface becomes stronger with a prolonged photocatalytic reaction. Hence, not only the calcination temperature increases the Ni adsorption strength on TiO$_2$, but also the photocatalytic process. Accordingly, the results show a clear adverse correlation between Ni adhesion and photocatalytic performance: the weaker the coordination of Ni, the more H$_2$ is generated.

2.2. Morphological Analysis

The morphology of the Ni/TiO$_2$ samples before and after HER was investigated by high-resolution transmission electron microscopy (HRTEM) and energy dispersive X-ray analysis (EDX) (figures shown in SI, Section 4.6). The HRTEM data show no apparent difference between the samples neither before and after HER nor to bare TiO$_2$. EDX analysis shows a homogenous Ni distribution for the as-prepared Ni/TiO$_2$ samples (before HER) and for RT and 400°C samples after HER. Yet, we see agglomeration of Ni in the PD sample – a phenomenon well known in the
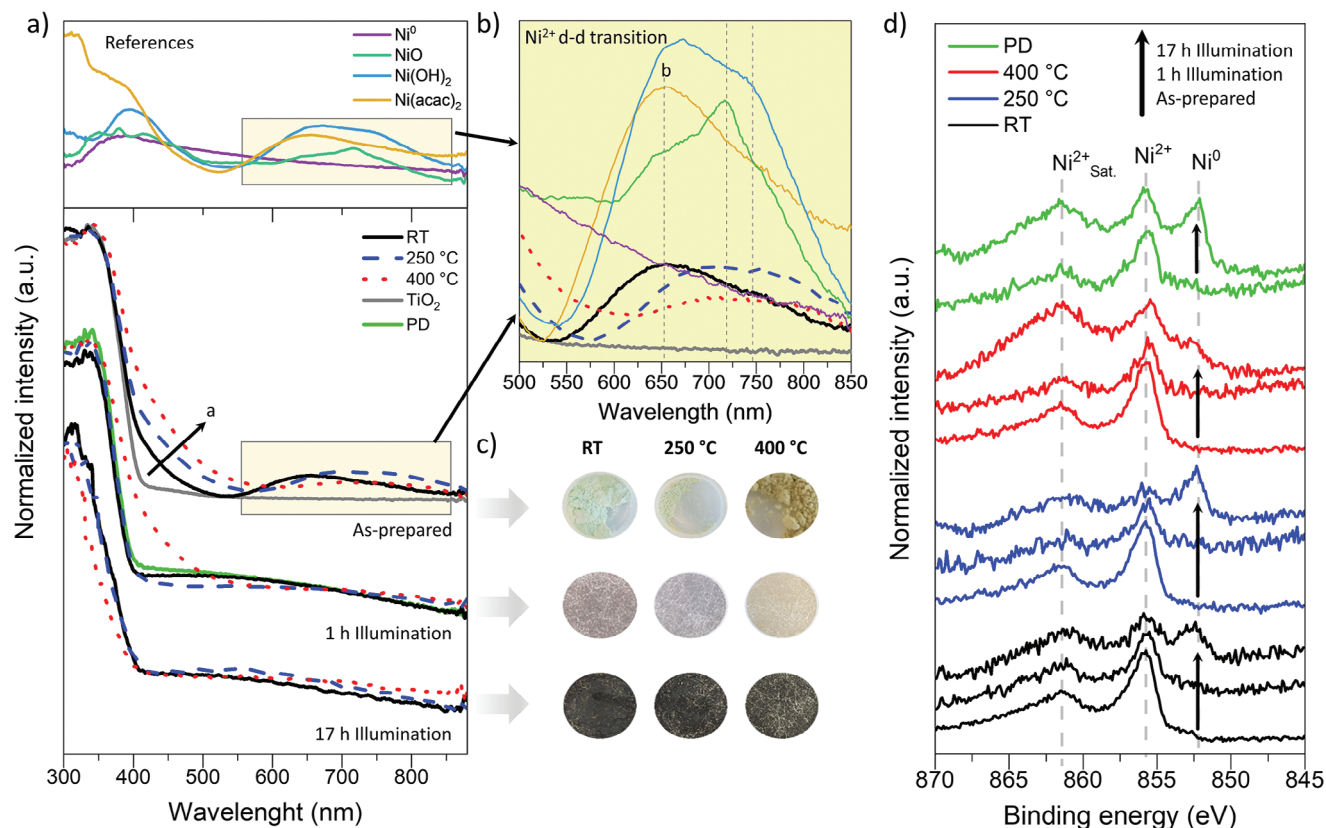
Figure 3. a) UV–vis of the as-prepared (i.e., before HER) Ni/TiO$_2$ samples prepared at different temperatures (non-calcined (RT), and calcined at 250 and 400°C), after the activation cycle (1 h illumination), after the stability-cycle (17 h illumination) – below – and reference spectra of relevant Ni compounds (above). b) Zoom-in of the 500 to 850 nm region. c) Digital photographs of all the relevant Ni/TiO$_2$ samples before HER and after the activation- and stability cycles. d) XPS Ni2p$_{3/2}$ detail spectra of the Ni/TiO$_2$ samples (RT, 250 and 400°C) before (as-prepared) and after HER (activation-, that is, 1 h illumination, and stability-cycle, that is, 17 h illumination), and of the PD sample after 1 and 17 h of illumination.

literature for the photodeposition process.[10,11,33] – as well as for the 250°C composite. These data confirm a homogenous atomic-size distribution of Ni on TiO$_2$, while for the PD and 250°C-after-HER sample, Ni generates a more dense packed area without forming clusters that are visible in HRTEM. Furthermore, the inconsistency of seeing more agglomeration at 250°C than at 400°C is possibly related to the intermediate adsorption strength (between RT and 400°C, as documented by XRF). This suggests that the adsorption of Ni at 250°C is weak enough so that Ni can diffuse along the TiO$_2$ surface, but strong enough so that it does not dissolve into the solution and randomly redeposits (such as in the case of the RT sample). Hereby, 250°C leads to the agglomeration of Ni species.

2.3. Ni Chemical State Analysis

We used ultraviolet-visible spectroscopy (UV–Vis spectroscopy) in diffuse reflection mode (DRS) to obtain insights about the chemical state, that is, chemical surrounding and oxidation state, of Ni before and after HER (**Figure 3**a). A set of references including Ni(acac)$_2$, NiO, Ni(OH)$_2$, and metallic Ni were used to complement the data. The pronounced absorption band below 400 nm – visible in all spectra mainly due to the presence of TiO$_2$ matrix

– corresponds to the ligand-to-metal charge transfer (LMCT) of oxygen (O^{2-}) to Ti^{4+}, that is, band-to-band excitation.[34,35]

The samples before HER show that the absorption edge shifts (in the as-prepared samples, in Figure 3a) to higher wavelengths with increasing calcination temperature, eventually extending the absorption range well above 500 nm. Such a shift has been related to the presence of dopants within the TiO$_2$ crystal lattice, which adds new energy levels within the band gap.[15,36–39] Alternatively, this apparent shift has also been attributed to interfacial charge transfer (IFCT) between the photoabsorber's (i.e., TiO$_2$) valence band (VB) and the surface-grafted metal species.[40–43] In both cases, the increase of the metal concentration (as an impurity in the lattice or grafted) is associated with an increase in absorption in this region. Since NiO, Ni(acac)$_2$ and Ni(OH)$_2$ references also show absorption in this region, we suggest that this absorption shift is likely due to a combination of (a) Ni(II) diffusion into TiO$_2$, which is facilitated by high-temperature calcination, (b) IFCT between the VB of TiO$_2$ and surface-grafted Ni(II) and (c) electronic transition of the Ni(II)-complexes formed on TiO$_2$ surface (e.g., Ni-OH or Ni-O species). Figure 3a,b show that in the range from 550 to 850 nm, all samples exhibit a characteristic Ni(II) (d^8) d–d transition band.[43,44] The exact spectral shape and the position of the absorption maximum are highly affected by the chemical environment of Ni(II) –, that is,

**ADVANCED
SCIENCE NEWS**

www.advancedsciencenews.com

**ADVANCED
MATERIALS
INTERFACES**

www.advmatinterfaces.de

coordination number, geometry, and nature of the neighboring atoms – as different ligands influence the ligand field and hence, the splitting and occupation of d-orbitals differently. The RT sample shows an absorption band similar to that of $Ni(acac)_2$ (b in Figure 3b), with a minor contribution of $Ni(OH)_2$ that likely arises from partial acac displacement upon adsorption onto TiO_2. For the 250°C sample, the band resembles more the $Ni(OH)_2$ reference, suggesting that a much larger portion of Ni species is now hydroxylated to the TiO_2 surface -OH groups, Ni-(OH)-Ti. This is in line with the partial oxidation of acac as observed in ATR-FTIR spectra of the composites, and aligns well with the stronger adhesion of Ni species to the TiO_2 surface, as suggested by the XRF leaching studies (Figures 1c and 2a). For the 400°C sample, the absorption band flattens, which suggests further hydroxylation or even formation of Ni-O-Ti bonds, due to possible diffusion of Ni ions into the TiO_2 lattice, suggested by the previously mentioned absorption shoulder, our previous work, and literature.[15,36–39]

The DRS data after 1 h illumination (activation cycle) reveals that the absorption shoulder in the 350 to 550 nm range vanishes for all samples except for the 400°C sample. This indicates that at 400°C the as-prepared Ni structure is partially preserved, which supports the diffusion of part of Ni into the TiO_2 lattice. Furthermore, the characteristic Ni(II) d–d transition in the 550 to 850 range disappears for all samples. This indicates the formation of Ni^0, which can also be suggested by the gradual color change of the catalyst powders after 1 h illumination and the matching DRS profile of the metallic Ni reference (Figure 3b,c).[19,25] After 17 h Illumination (stability-cycle), all DRS spectra and the color of the samples look similar (Figure 3a,c), which indicates that all samples have transformed to a similar chemical state and composition.

The samples were further investigated by X-ray photoelectron spectroscopy (XPS) before and after HER (both activation- and stability-cycle). Briefly, all survey spectra show the expected C1s, O1s, Ti2p, and Ni2p components. The detailed spectra of the C1s and O1s belong to the acac anion and the characteristic adventitious carbon. The Ti2p spectra show no differences before and after HER, with a typical Ti^{4+} spectral shape at a binding energy of 458.5 eV ($Ti2p_{2/3}$), which further excludes a potential contribution of TiO_2 transformation to the observed HER profiles, also confirmed by XRD (all corresponding XPS graphs are shown in the SI section 4.7 and XRD in Figure S13). Yet, as preluded by DRS data, the photocatalysts show substantial differences in their $Ni2p_{3/2}$ lines. Figure 3d indicates that before HER (in the as-prepared samples) no apparent changes are induced by the different thermal treatments. The main $Ni2p_{3/2}$ peak has a binding energy (BE) of 855.8 eV and a small shoulder ~852.8 eV, typical values for Ni^{2+} and Ni^0, respectively.[23,45–47] Based on the DRS data, the spectral fitting parameters proposed by Biesinger et. al.[47] and according to the measured BEs, the most probable chemical surrounding for Ni in our Ni/TiO_2 samples can be attributed to a combination of Ni-OH and metallic Ni, with a contribution of the latter one of 17, 26, and 13 at% for the RT, 250 and 400°C samples, respectively (see SI, section 4.7.5 for more details). Therefore, we can conclude that the main Ni species for the as-prepared samples is Ni^{2+} – in the form of Ni-OH or Ni-acac for the RT sample and with a higher contribution of Ni-OH with increasing calcination temperature – and Ni^0.

For the samples after 1 h illumination (activation cycle), the $Ni2p_{3/2}$ spectra show no major differences between the samples, with the Ni oxidation state still being Ni^{2+} as the main species and with small amounts of Ni^0, yet with an increased proportion of metallic Ni in all samples (see SI, section 4.7.5). However, after 17 h illumination (stability cycle), we observe major differences among the samples with a clear Ni^0 signal intensity increase. In more detail, the RT and PD samples show a similar Ni^{2+}:Ni^0 intensity ratio – that is, the relative amount of Ni^{2+} and Ni^0 – indicating that Ni^0 becomes the dominant species. Furthermore, the similarity among the samples, also seen in DRS (Figure 3a, 1 h illumination) indicates a similar Ni^{2+}/Ni^0 formation mechanism. For the 250°C sample, the Ni^0 signal is much more intense than the Ni^{2+} signal, indicating that in this sample even more Ni^0 was generated than in the RT sample. Then at 400°C, the opposite is observable: the Ni^0 peak intensity is less than Ni^{2+}. In connection with these observations and the information provided by XRF and EDX, the most probable explanation, again, is the adsorption strength of Ni to TiO_2. Consequently, in the RT sample, Ni is weakly adsorbed, thus Ni can undergo an efficient redox shuttle (transformation of Ni^{2+} to Ni^0 and back by reacting with H^+ to H_2, $Ni^{2+} \leftrightarrow Ni^0$), as the Ni oxidation state is not stabilized by the adsorption to TiO_2, but still strong enough for electron transfer. At 250°C, Ni starts to get strongly adsorbed (most likely via partial chemical coordination or physisorption), thus enabling efficient electron transfer (more Ni^{2+} gets reduced) and stabilizing Ni^0 on the TiO_2 lattice (still not strong enough to inhibit Ni^0 migration and agglomeration, seen in EDX). At 400°C, Ni is even more strongly adsorbed (increasing the chemisorption character), being less prone to structural changes. Hence, Ni^{2+} is partially stabilized by the TiO_2 lattice hindering its reduction to Ni^0, its migration, and agglomeration.

In summary, the DRS and XPS data show that the main Ni species before HER is Ni^{2+} – in the form of Ni-acac and Ni-OH – with a minor contribution of Ni^0. After the activation cycle (1 h of HER) the system only slightly increases its metallic Ni content, while after the stability cycle (17 h of HER) most of the Ni^{2+} (mainly in the form of Ni-O-Ti and Ni-(OH)-Ti) gets converted into metallic Ni. This transformation seems independent of the calcination temperature but occurs with a different efficiency (250 °C >RT >400 °C). Hence, these results indicate the in-situ formation of metallic Ni from Ni^{2+} upon photocatalytic turnover conditions, but with a different efficiency upon calcination.

2.4. Proposed Mechanism

It is well-accepted in the literature that Ni^0 constitutes the active HER center.[10,11,16,17,19–22,27,33] Furthermore, numerous studies have demonstrated the transformation of Ni^{2+} to Ni^0 upon illumination when in presence of an electron donor. Additionally, photo deposition experiments showed how dissolved Ni^{2+} is able to react with a photo-excited electron and deposit on the substrate.[10,11,16,17,27] Hereby, integrating insights from the literature with the findings presented in this study, we can propose a photocatalytic HER active Ni state formation mechanism and the effects of increasing pre-calcination temperature on the
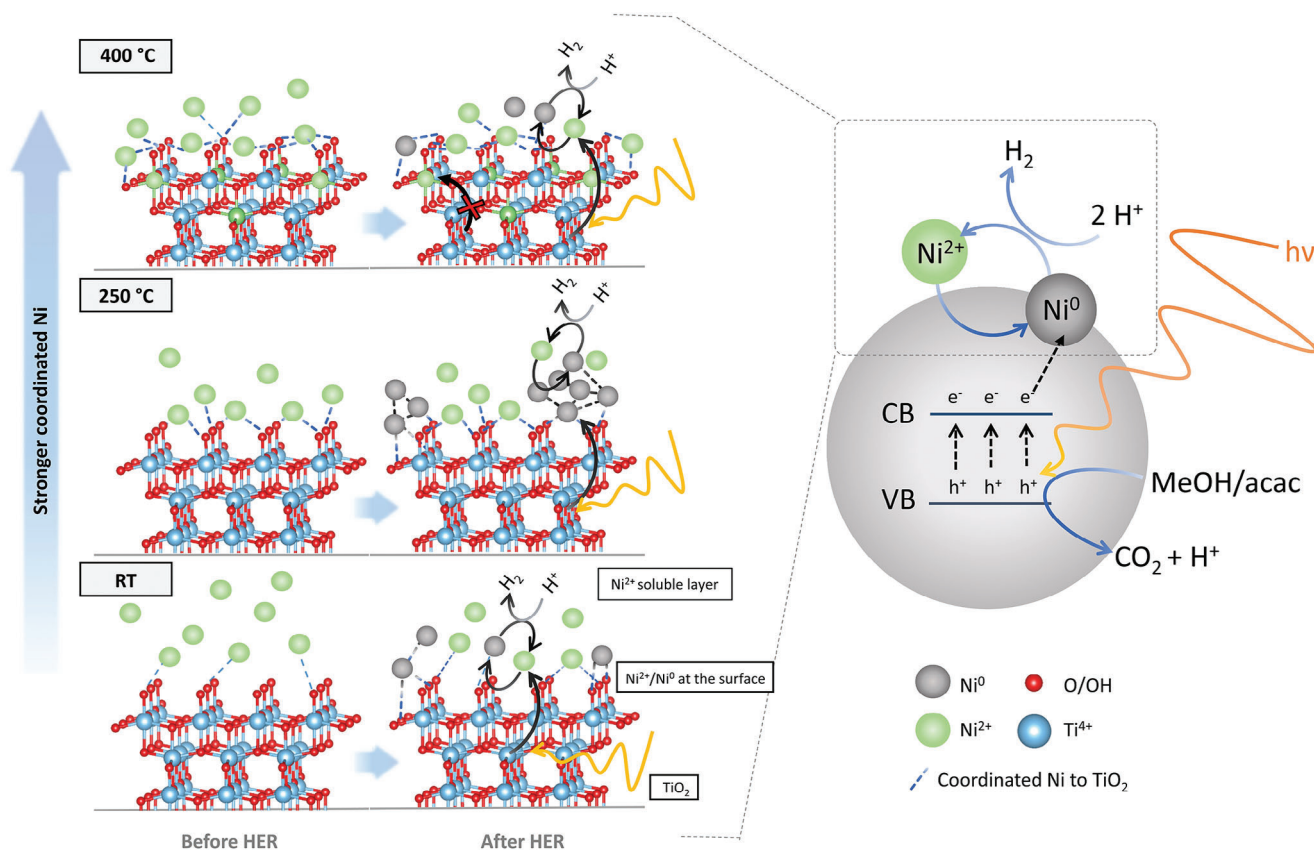
Figure 4. Proposed photocatalytic mechanism and schematic of the Ni/TiO$_2$ system for the case of the non-calcined (RT) and calcined Ni/TiO$_2$ samples (at 250 and 400°C) showing the states of the photocatalytic surface for the as-prepared samples –, that is, before HER – and after the photocatalytic reaction –, that is, after HER.

photocatalyst's structure and HER activity. Summarizing the key findings of this study as obtained by XRF, TEM/EDX, UV–vis, and XPS:

1. With increasing temperature, the performance of Ni/TiO$_2$ in HER decreases, coinciding with stronger Ni adhesion/adsorption onto TiO$_2$, as indicated by XRF analysis.
2. During photocatalysis, the efficiency of Ni^{2+} to Ni^0 reduction follows the sequence 250°C > RT/PD > 400°C, as revealed by DRS and XPS.
3. At 400°C, the oxidation state of Ni^{2+} is stabilized within the TiO$_2$ lattice, while at 250°C, Ni^0 dominates, as indicated by DRS and XPS.
4. RT and PD samples exhibit consistent patterns across various data sets (HER, UV–vis, XPS), indicating similarities in the composition and structure of the Ni active state.

By correlating these observations with the HER performance, existing literature, and a two-step photo-transformation of Ni on the TiO$_2$ surface:

$$Ni^{2+} + 2e^- \xrightarrow{(I)} Ni^0 \qquad (1)$$

$$Ni^0 + 2 H^+ \xrightarrow{(II)} Ni^{2+} + H_2 \qquad (2)$$
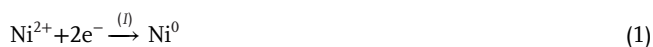
involving Ni photoreduction and electron release to form H$_2$, we can propose a formation mechanism of the active Ni species during HER as summarized in **Figure 4**.

Figure 4, the RT sample demonstrates weak physisorption of Ni^{2+} species, which are capable of re-dissolving into the solution during the photocatalytic reaction. Similar to the photodeposition process observed in the PD sample, these re-dissolved Ni species then get photodeposited back onto the TiO$_2$ surface in the form of Ni^0 through a reaction with the photogenerated electrons in TiO$_2$ (Ni undergoes reaction step I). Subsequently, H$^+$ generated from the decomposition of MeOH/acac gets adsorbed onto Ni^0 centers and reduced to H$_2$, which ultimately regenerates the Ni^{2+} state (Ni undergoes reaction step II).

At the calcination temperature of 250°C (Figure 4, 250°C), stronger Ni adsorption takes place, leading to a partial chemisorption character of the anchoring and stronger electronic communication with TiO$_2$. Consequently, more electrons can be conducted through this Ni/TiO$_2$ interface, resulting in an increased degree of Ni reduction. Hence, Ni^0 is stabilized on the TiO$_2$ surface and continues to grow, acting as an efficient electron trap increasing the Ni^0 content and the undesired growth and agglomeration. That means, at 250°C the reaction step II is partially inhibited, leading to a Ni^0 accumulation and less efficient HER performance.

At 400°C (Figure 4, 400 °C), we observe that Ni is much stronger adsorbed to the surface -OH/-O groups, with an increased chemisorption character. Additionally, Ni is partially incorporated into the TiO_2 lattice (likely its sub-surface), which leads to a stabilization of the Ni^{2+} state. As a result, reaction step I is partially hindered, and less Ni^0 is generated leading to a drop in HER performance.

In summary, for effective extraction of photoelectrons from the TiO_2 support and their injection into adsorbed H^+ to generate H_2, it is crucial for Ni to be weakly adsorbed/adhered to the TiO_2 surface. In this situation, Ni species facilitate a dynamic and reversible redox shuttling ($Ni^{2+} \leftrightarrow Ni^0$) of the electrons between TiO_2 and reactants, similar to the case observed in Ni/TiO_2 samples prepared via Ni photo deposition.[10,11,48] In contrast, when Ni species are strongly adhered to the TiO_2 surface, either by becoming a part of the TiO_2 lattice or by transforming into Ni^0 aggregates, this dynamic process is partially hindered. In such cases, Ni centers are limited in their ability to undergo redox shuttling, resulting in the less efficient transformation between Ni^{2+} and Ni^0 states, which consequently, limits their photocatalytic performance.

3. Conclusion

In this study, we demonstrate that post-synthesis calcination of the photocatalyst can negatively impact its photocatalytic performance. Ni, acting as a co-catalyst, was grafted onto TiO_2 nanoparticles (Ni/TiO_2) using a wet impregnation method and then subjected to calcination at 250 and 400°C. The non-calcined Ni/TiO_2 sample (RT) exhibited the highest performance, with a gradual decrease in hydrogen generation as the calcination temperature increased (RT >250°C >400°C). XRF analysis and Ni washing experiments revealed that the primary cause of this effect is the increase in the adsorption strength of Ni on the TiO_2 surface. As the calcination temperature increases, Ni becomes more strongly adsorbed (RT <250°C< 400°C), hindering its ability to efficiently undergo a redox shuttle (transformation of Ni^{2+} to Ni^0 and back after reaction with H^+ to H_2, that is, $Ni^{2+} \leftrightarrow Ni^0$) required to generate H_2 efficiently. At 250°C, Ni^{2+} adsorption becomes strong enough to facilitate efficient electron transfer between TiO_2 and Ni^{2+}, leading to agglomeration of Ni^0 and acting as an electron sink, thereby inhibiting the dynamic $Ni^{2+} \leftrightarrow Ni^0$ shuttle. At 400°C, Ni establishes even stronger adsorption with TiO_2, stabilizing the Ni^{2+} state and preventing the formation of Ni^0. Thus, the stabilizing effect of Ni^{2+} or Ni^0 in the various calcined samples detrimentally affects the overall photocatalytic performance. Hereby, this work underscores that not only Ni^0 plays a key role in enabling efficient HER performance, but also the right $Ni^{2+}:Ni^0$ ratio which enables dynamic and efficient $Ni^{2+} \leftrightarrow Ni^0$ shuttling. These findings emphasize that possible side effects of chosen calcination and synthetic methodologies need to be considered when designing a range of photocatalytic materials.

4. Experimental Section

Synthesis of the Composites: All materials used for the syntheses were obtained from commercial suppliers: anatase TiO_2 and $Ni(acac)_2$ from Sigma–Aldrich; absolute ethanol was used for the synthesis (from Chem-

Lab NV); deionized water and HPLC-gradient grade methanol (from VWR) were used for the photocatalytic experiments. The composites were synthesized by a wet impregnation method with post-synthetic thermal treatments conducted in ambient air. The general synthesis procedure used for all samples included a) suspending the TiO_2 powder (12.5 mmol) in 20 ml of the corresponding solvent (ethanol or water). b) Next, the $Ni(acac)_2$ (0.626 mmol) was dissolved separately in the corresponding solvent (70 ml for H_2O and 50 ml for EtOH) and sonicated for 5 min. c) The two solutions were then mixed and sonicated for 10 min. d) The sample prepared under air (EtOH/air) was left stirring at 60°C until complete evaporation of the solvent took place, while the vacuum samples (EtOH/vacuum and H_2O/vacuum) the solvent were extracted by a rotary evaporator. e) The remaining powder was then collected and ground. f) Afterward, the samples were heat-treated in ambient air at the corresponding temperature (no heat treatment (RT), 250 or 400°C) with a heating ramp of 2 h to reach the desired temperature, and then allowed to naturally cool down. In the case of the photodeposited sample (PD), TiO_2 (0.11 mmol) was suspended in a 50:50 vol% MeOH-water solution and a $Ni(acac)_2$ stock solution was added aiming for 5 at.% Ni. Next, the standard photocatalytic experiments were carried out to allow in situ deposition of Ni on TiO_2 and simultaneous H_2 detection (see photocatalytic experiment section for details). For the washing experiments, the corresponding samples were suspended in a 10 ml MeOH: H_2O solution (the same solution as for the HER). After stirring for 5 min, the suspensions were vacuum-filtered and dried under vacuum-yielding powders for XRF analyses.

Photocatalytic Experiments: Hydrogen evolution experiments were performed using a side irradiation gas-flow slurry type home-made reactor equipped with an LED lamp light source centered at 365 ± 20 nm (Thorlabs) (Figure S1) and an in situ product detection system. In a single experiment, 10 mg of the powdered photocatalyst was dispersed in 10 ml 50:50 vol% MeOH-water solution. During the experiment, the reactor was continuously purged with argon (flow rate of 15 ml min^{-1}, controlled with a mass flow controller from MCC-Instruments) to deliver the gaseous products to the online gas analyzer (X-Stream, Emerson Process Management) equipped with a thermal conductivity detector (TCD) for H_2 quantification and a photometric non-dispersive IR sensor for CO_2 detection. The temperature of the reactor was kept constant at 15°C through a water-cooling system (Lauda). The 3 min delay between the start of illumination and the rise of hydrogen signal in all H_2 and CO_2 rate graphs was due to the experimental setup as the carrier gas (Ar) needs a certain time to reach from the reactor to the detector (see Figure S1).

Characterization Methods: Transmission electron microscopy (TEM) images were obtained using the FEI TECNAI F20 transmission electron microscope equipped with a field emission gun in bright field mode using 200 kV acceleration voltage. The sample was prepared from an ethanol suspension, using a copper holey carbon-coated grid (Plano, 200 mesh). The EDX mapping was performed with the same device in scanning mode with approximately 2 nm resolution and high-angle annular dark-field imaging (HAADF) equipped with an EDAX-AMETEK Apollo XLTW SDD EDX-detector. The chemical composition of the samples was obtained with X-ray photoelectron spectroscopy (XPS). All measurements were carried out with the sample at normal emission angle to the analyzer. The samples were mounted onto the sample holder using double-sided carbon tape and In-foil. The XPS spectra were acquired using an Axis Ultra DLD instrument from Kratos Analytical (UK) with the base pressure during spectra acquisition better than 1.1×10^{-9} Torr (1.5×10^{-7} Pa), achieved by a combination of turbomolecular and ion pumps. Monochromatic Al-Kα radiation ($h\nu = 1486.6$ eV) is employed with the anode power set to 150 W. All spectra were collected at normal emission angle. Data analysis was done using the CasaXPS Version 2.3.19PR1.0 software package employing Shirley/Shirley Tougaard backgrounds and Scofield sensitivity factors.[49,50] Curve fits using combined Gaussian–Lorentzian peak shapes (GL(30)) were used to discern the components of detail spectra, except for the metallic Ni where an asymmetric LA(1.1,2.2,10) line shape was used. The binding energy scale was calibrated using sputter-etched Au, Ag, and Cu standard samples, which exhibit Au $4f_{7/2}$, Ag $3d_{5/2}$, and Cu $2p_{3/2}$ peak positions at 83.96 eV, 368.21 eV, and 932.62 eV, respectively. Hence, all binding energies was given to the calibrated Fermi level

at 0 eV. All content values were shown in units of a relative atomic percent (at%), where the detection limit in survey measurements usually lies around 0.1–0.5 at%, depending on the element. The accuracy of XPS measurements is around 10–20% of the values shown. Assignment of different components was primarily done using Refs.[51,52] For the attenuated total reflection Fourier–transform Infrared spectroscopy (ATR-FTIR) measurements a PerkinElmer FTIR Spectral UATR-TWO with a spectrum two Universal ATR (Single Reflection Diamond) accessory was used. The X-ray Fluorescence Spectroscopy (XRF) chemical quantification analysis was performed with an Atomika 8030C X-ray fluorescence analyzer with a Molybdenum X-ray source monochromitized Kα-line. The excitation conditions were 50 kV and 47 mA, 100 s with a total reflection geometry and an Energy-dispersive Si(Li)-detector. For the sample preparation, all reflectors were washed thoroughly and measured to account for true blanks. 1 miligram of the solid nano-powder was loaded on the clean reflectors and sealed with 5 µL of a 1% PVA solution to avoid contamination of the detector. After drying for 5 min on a hot plate and cooling, the reflectors with the loaded samples were measured. For the data evaluation, Ti was set as a matrix with 100% (wt%), and relative amounts of Ni were acquired (wt%). The accuracy of XRF measurements was ≈10% of the values shown. An exemplary XRF spectrum of a Ni/TiO_2 sample is shown in Figure S12. For the Diffuse Reflectance Ultraviolet Spectroscopy (DRS or DR-UV–vis) a Jasco V-670 UV–vis photo spectrometer was used and the reflectance spectra of the catalyst powders were acquired using an integration sphere accessory. The X-ray diffraction (XRD) was performed using an XPERT II: PANalytical XPert Pro MPD (Θ-Θ Diffractometer) for the experiments. The sample was placed on a sample holder and irradiated with a Cu X-ray source (8.04 keV, 1.5406 Å). The signal was acquired with Bragg-Brentano Θ/Θ-diffractometer geometry ranging from 5° to 80° degrees. The detector system was a semiconductor X'Celerator (2.1°) detector.

Supporting Information

Supporting Information is available from the Wiley Online Library or from the author.

Conflict of Interest

The authors declare no conflict of interest.

Data Availability Statement

The data that support the findings of this study are available from the corresponding author upon reasonable request.

[1] S. Zhu, D. Wang, *Adv. Energy Mater.* **2017**, *7*, 1700841.

[2] K. Takanabe, *ACS Catal.* **2017**, *7*, 8006.

[3] S. J. A. Moniz, S. A. Shevlin, D. J. Martin, Z.-X. Guo, J. Tang, *Energy Environ. Sci.* **2015**, *8*, 731.

[4] F. E. Osterloh, *ACS Energy Lett.* **2017**, *2*, 445.

[5] Y. Zhong, C. Peng, Z. He, D. Chen, H. Jia, J. Zhang, H. Ding, X. Wu, *Catal. Sci. Technol.* **2021**, *11*, 27.

[6] X. Li, J. Yu, J. Low, Y. Fang, J. Xiao, X. Chen, *J. Mater. Chem. A* **2015**, *3*, 2485.

[7] T. Liu, L. Bai, N. Tian, J. Liu, Y. Zhang, H. Huang, *Int. J. Hydrog. Energy* **2023**, *48*, 12257.

[8] R. Marschall, *Adv. Funct. Mater.* **2014**, *24*, 2421.

[9] M. R. Nellist, F. A. L. Laskowski, F. Lin, T. J. Mills, S. W. Boettcher, *Acc. Chem. Res.* **2016**, *49*, 733.

[10] H. Zhao, Q. Mao, L. Jian, Y. Dong, Y. Zhu, *Chin. J. Catal.* **2022**, *43*, 1774.

[11] K. Wenderich, G. Mul, *Chem. Rev.* **2016**, *116*, 14587.

[12] P. Ciambelli, G. L. Guardia, L. Vitale, *Stud. Surf. Sci. Catal.* **2020**, *179*, 97.

[13] K. P. de Jong, *Synthesis of Solid Catalysts*, Wiley, Hoboken, NJ **2009**.

[14] P. Ayala, A. Giesriegl, S. P. Nandan, S. N. Myakala, P. Wobrauschek, A. Cherevan, *Catalysts* **2021**, *11*, 417.

[15] J. S. Schubert, L. Kalantari, A. Lechner, A. Giesriegl, S. P. Nandan, P. Alaya, S. Kashiwaya, M. Sauer, A. Foelske, J. Rosen, P. Blaha, A. Cherevan, D. Eder, *J. Mater. Chem. A* **2021**, *9*, 21958.

[16] X. Liu, H. Zhuang, *Int. J. Energy Res.* **2021**, *45*, 1480.

[17] Y. Xu, R. Xu, *Appl. Surf. Sci.* **2015**, *351*, 779.

[18] R. Shen, J. Xie, Q. Xiang, X. Chen, J. Jiang, X. Li, *Chin. J. Catal.* **2019**, *40*, 240.

[19] W.-T. Chen, A. Chan, D. Sun-Waterhouse, T. Moriga, H. Idriss, G. I. N. Waterhouse, *J. Catal.* **2015**, *326*, 43.

[20] A. Indra, P. W. Menezes, K. Kailasam, D. Hollmann, M. Schröder, A. Thomas, A. Brückner, M. Driess, *Chem. Commun.* **2015**, *52*, 104.

[21] J. Yu, Y. Hai, B. Cheng, *J. Phys. Chem. C* **2011**, *115*, 4953.

[22] S. Lv, M. Pei, Y. Liu, Z. Si, X. Wu, R. Ran, D. Weng, F. Kang, *Nano Res.* **2022**, *15*, 5848.

[23] J. S. Schubert, J. Popovic, G. M. Haselmann, S. P. Nandan, J. Wang, A. Giesriegl, A. S. Cherevan, D. Eder, *J. Mater. Chem. A* **2019**, *7*, 18568.

[24] X. Chen, J. Xiong, J. Shi, S. Xia, S. Gui, W. Shangguan, *Front. Energy* **2019**, *13*, 684.

[25] A. L. Luna, D. Dragoe, K. Wang, P. Beaunier, E. Kowalska, B. Ohtani, D. Bahena Uribe, M. A. Valenzuela, H. Remita, C. Colbeau-Justin, *J. Phys. Chem. C* **2017**, *121*, 14302.

[26] J. L. Rodríguez, F. Pola, M. A. Valenzuela, T. Poznyak, *MRS Online Proc. Libr.* **2011**, *1279*, 53.

[27] W. Wang, S. Liu, L. Nie, B. Cheng, J. Yu, *Phys. Chem. Chem. Phys.* **2013**, *15*, 12033.

[28] M. Sakamoto, M. Fujistuka, T. Majima, *J. Photochem. Photobiol. C Photochem. Rev.* **2009**, *10*, 33.

[29] W.-C. Lin, W.-D. Yang, I.-L. Huang, T.-S. Wu, Z.-J. Chung, *Energy Fuels* **2009**, *23*, 2192.

[30] J. Schneider, D. W. Bahnemann, *J. Phys. Chem. Lett.* **2013**, *4*, 3479.

[31] V. Kumaravel, M. Imam, A. Badreldin, R. Chava, J. Do, M. Kang, A. Abdel-Wahab, *Catalysts* **2019**, *9*, 276.

[32] D. L. Howard, H. G. Kjaergaard, J. Huang, M. Meuwly, *J. Phys. Chem. A* **2015**, *119*, 7980.

[33] S. Sun, Y.-C. Zhang, G. Shen, Y. Wang, X. Liu, Z. Duan, L. Pan, X. Zhang, J.-J. Zou, *Appl Catal B* **2019**, *243*, 253.

[34] X. Qiu, M. Miyauchi, K. Sunada, M. Minoshima, M. Liu, Y. Lu, D. Li, Y. Shimodaira, Y. Hosogi, Y. Kuroda, K. Hashimoto, *ACS Nano* **2012**, *6*, 1609.

[35] L. P. Bevy, *Trends in Catalysis Research*, Nova Publishers, Hauppauge, New York **2006**.

[36] M. Myilsamy, M. Mahalakshmi, V. Murugesan, N. Subha, *Appl. Surf. Sci.* **2015**, *342*, 1.

[37] S. Akel, R. Boughaled, R. Dillert, M. El Azzouzi, D. W. Bahnemann, *Molecules* **2020**, *25*, 249.

[38] H. Yu, J. Tian, F. Chen, P. Wang, X. Wang, *Sci. Rep.* **2015**, *5*, 13083.

[39] J. Choi, H. Park, M. R. Hoffmann, *J. Mater. Res.* **2010**, *25*, 149.

[40] H. Yu, H. Irie, K. Hashimoto, *J. Am. Chem. Soc.* **2010**, *132*, 6898.

[41] H. Irie, K. Kamiya, T. Shibanuma, S. Miura, D. A. Tryk, T. Yokoyama, K. Hashimoto, *J. Phys. Chem. C* **2009**, *113*, 10761.

[42] H. Irie, S. Miura, K. Kamiya, K. Hashimoto, *Chem. Phys. Lett.* **2008**, *457*, 202.

[43] X. Cai, Y. Cai, Y. Liu, S. Deng, Y. Wang, Y. Wang, I. Djerdj, *Ceram. Int.* **2014**, *40*, 57.

[44] E. Gallo, E. Gorelov, A. A. Guda, A. L. Bugaev, F. Bonino, E. Borfecchia, G. Ricchiardi, D. Gianolio, S. Chavan, C. Lamberti, *Inorg. Chem.* **2017**, *56*, 14408.

[45] M. C. Biesinger, L. W. M. Lau, A. R. Gerson, R. S. C. Smart, *Phys. Chem. Chem. Phys.* **2012**, *14*, 2434.

[46] M. C. Biesinger, *Surf. Interface Anal.* **2017**, *49*, 1325.

[47] M. C. Biesinger, B. P. Payne, A. P. Grosvenor, L. W. M. Lau, A. R. Gerson, R. S. C. Smart, *Appl. Surf. Sci.* **2011**, *257*, 2717.

[48] S. Kumar, K. Ojha, A. K. Ganguli, *Adv. Mater. Interfaces* **2017**, *4*, 1600981.

[49] S. Tougaard, *Surf. Interface Anal.* **1997**, *25*, 137.

[50] D. A. Shirley, *Phys. Rev. B* **1972**, *5*, 4709.

[51] C. D. Wagner, A. V. Naumkin, A. Kraut-Vass, J. W. Allison, C. J. Powell, J. R. Rumble, **2003**.

[52] D. Briggs, G. Beamson, *Anal. Chem.* **1992**, *64*, 1729.